



Synthesis, characterization, thermal, and antibacterial activity studies on MgO powders

Selim Demirci¹ · Berceç Kiran Yildirim² · Mehmet Masum Tünçay¹ · Nusret Kaya³ · Arif Nihat Güllüoğlu¹

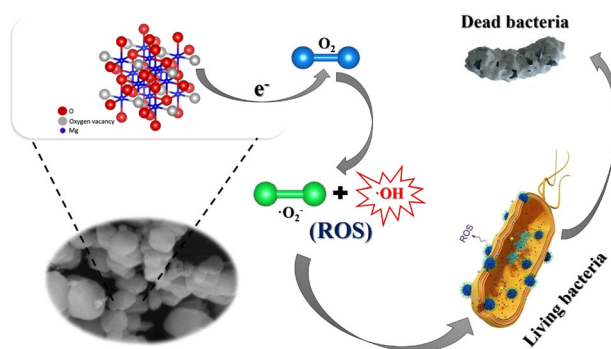
Received: 28 May 2021 / Accepted: 5 August 2021 / Published online: 17 August 2021

© The Author(s), under exclusive licence to Springer Science+Business Media, LLC, part of Springer Nature 2021

Abstract

In this study, MgO particles were synthesized via sol–gel technique and calcined at 600 °C for 2 h with heating rates of 2, 5, 10, and 20 °C/min, respectively, for the first time. Comprehensive characterizations were performed by TGA-DTA, XRD, SEM, Raman spectroscopy, BET analysis, photoluminescence techniques. The kinetic parameters were determined by employing four popular model-free methods: Flynn–Wall–Ozawa (FWO), Kissinger–Akahira–Sonuse (KAS), Starink, and Tang methods. MgO powders had a high crystalline structure regardless of different heating rates based on XRD results. Surface morphologies and surface areas of MgO powders did not change with heating rates. Surface morphologies of MgO powders were found to be nearly spherical with some rounded shape and exhibiting faceted edges in some regions. The specific surface area of MgO powders was found to be 5.9179, 5.6883, 3.6617, and 4.1942 m²/g with increasing heating rate, respectively. According to Raman analysis, MgO particles produced at 2 °C/min possessed higher surface defects like oxygen vacancies. The PL emission signals for MgO particles were observed at ~500 nm consisting of broad peaks, which might be attributed to oxygen defects on the surface of particles. The antibacterial performances of MgO particles were carried out against gram-negative *E. coli* and gram-positive *B. subtilis* by means of the agar disc diffusion method. MgO particles produced at a heating rate of 2 °C/min possessed the biggest inhibition zone against gram-positive *B. subtilis*. Having better antibacterial performances for MgO particles produced at 2 °C/min heating rate might be attributed to surface oxygen vacancies and surface area, which led to the generation of more reactive oxygen species (ROS).

Graphical Abstract



Keywords MgO particles · Sol–gel method · Antibacterial activity · Thermodynamic properties · Heating rate

✉ Selim Demirci
selim.demirci@marmara.edu.tr

¹ Faculty of Engineering, Department of Metallurgical and Materials Engineering, Marmara University, Kadikoy, 34722 Istanbul, Turkey

² Faculty of Engineering, Department of Chemical Engineering, Marmara University, Kadikoy, 34722 Istanbul, Turkey

³ Faculty of Engineering, Department of Materials Science and Engineering, Izmir Katip Celebi University, Çiğli, 35620 Izmir, Turkey

Highlights

- MgO powders were fabricated by the sol–gel process with different heating rates.
- The effect of the heating rate on structure, morphology, and antibacterial activity was investigated.
- Non-isothermal and thermodynamic parameters of MgO powders were studied.
- MgO sample prepared at 2 °C/min heating rate exhibited the best antibacterial performance.

1 Introduction

Numerous researches have been done about the antibacterial activity of metal oxide nanoscale range materials in order to understand and predict their mechanism in terms of bacteria and surface interactions so far [1]. Among the nanoscale range metal oxides, MgO (magnesium oxide) is one of the common oxide which has been gained tremendous attention owing to its crucial properties such as low cost, abundance, excellent thermal stability, non-toxicity, and biodegradability [2–6]. MgO has intensively been utilized in different application fields such as catalyst [7, 8], refractory materials [9], hazardous waste remediation [10], paints and superconductors [11], adsorption [12], and antibacterial or antimicrobial agents [13] due to its unique properties mentioned above. From all of the mentioned application areas, the antibacterial activity area has been drawn considerable attention for MgO. MgO possesses superior antibacterial activity. That is why MgO is regarded as an efficient antibacterial agent versus Gram-positive and Gram-negative bacteria without illumination [14]. The antibacterial mechanism of MgO particles depends on the generation of reactive oxygen species (ROS). The presence of ROS leads to oxidative stress on bacterial cells. The strong oxidative stress causes damage to the biological system in order to destroy and kill them. The production of ROS occurs between the bacteria and MgO nanoparticle surfaces. When the MgO nanoparticle surfaces react with absorbed O₂ originated from bacteria, superoxide radicals (O₂⁻) are formed because of surface defects such as oxygen vacancies at the surface of MgO nanoparticles [15–17]. The capability of ROS generation is directly related to intrinsic properties of MgO nanoparticles such as size, morphology, crystallinity, composition, which cause changing of oxygen vacancy concentration and basicity of MgO nanoparticles at the surfaces [18, 19]. The intrinsic properties of MgO nanoparticles can be varied by synthesis route and processing conditions such as different production methods or calcination temperatures. There are numerous various types of methods in order to fabricate MgO nanoparticles, such as hydrothermal [20], solvothermal [21], co-precipitation [22], microwave-assisted [23], sol–gel [24], combustion [25], etc. Amongst, the sol–gel technique is a very simple, eco-friendly, and low-cost method in order to prepare MgO nanoparticles. Up to now, numerous studies have been reported about MgO nanoparticles prepared with different

modifications such as doping, morphology, heterostructure, calcination parameters (temperature, time) by using the sol–gel method in order to evaluate antibacterial activity of MgO nanoparticles. For example, Rao et al. [5] investigated the effect of various ions doping in MgO nanoparticles on antibacterial activity. Anicic et al. [26] reported the influence of the calcination temperature on antibacterial characteristics of MgO microrods. Cai et al. [27] evaluated the impact of the amount of Ag doping in MgO nanoparticles on antibacterial activities. Wang et al. [28] produced MgO-carboxymethyl chitosan nanocomposite to investigate antibacterial activities. As mentioned above, MgO particles with different modifications were produced by the sol–gel method to understand and figure out antibacterial activity. To the best of our knowledge, there is no study or report about the synthesis of MgO nanoscale particles at different heating rates in order to observe antibacterial activity by using the sol–gel method. Even though Jeevanandam et al. [29] focused on the effect of calcination temperature on the MgO nanoparticles synthesized by sol–gel method, the influence of heating rate on the physicochemical properties of MgO nanoparticles have not investigated yet. But there are some studies that state the importance of the heating rate on the physical and chemical properties of particles. Dikici et al. [30] studied on the effect of heating rate on photocatalytic degradation for TiO₂ oxides. They found that heating rate changed the degree of crystallization of TiO₂ oxides, which led to alteration of the photocatalytic degradation efficiency. Demirci et al. [31] investigated how the heating rate influenced the microstructure and surface properties of ZnO nanoparticles. The findings showed that the heating rate regime caused the variation of physical properties of ZnO particles such as surface oxygen vacancies. Increasing of heating rate generated high surface oxygen vacancies, which shifted the photocatalytic degradation rate. Therefore, this study investigated the effect of different heating rates on the crystalline structure of MgO nanoscale particles formed by the sol–gel technique. Furthermore, kinetic and thermodynamic studies were performed for MgO nanoscale particles. The physical and chemical properties of MgO nanoscale particles such as crystalline structure, surface morphology, surface defect, etc. were characterized by using XRD, FESEM, EDS, Raman spectrum, photoluminescence (PL), BET analysis. Moreover, the antibacterial activity of MgO powders was examined.

2 Material and methods

2.1 Synthesis of MgO particles

MgO powders were prepared via the sol–gel method, as described earlier, with slight modifications of our previous study [8]. Magnesium nitrate hexahydrate ($\text{Mg}(\text{NO}_3)_2 \cdot 6\text{H}_2\text{O}$, 98%, Telkim) was used as an initial material. First, 102.33 g of magnesium nitrate hexahydrate was weighed then dissolved in 100 mL absolute ethanol (purchased from Merk Company) for 30 min. Then, 20 ml of GAA (glacial acetic acid) was added to the obtained solution and vigorously stirred. Then, the prepared solution was dried at 150 °C for 24 h in order to get the xerogel structure. The calcination of xerogel powders was performed at 600 °C for 2 h at different heating rates. 2, 5, 10, and 20 °C/min were chosen as heating rates to get MgO powders.

2.2 Material characterization

2.2.1 Thermogravimetric and differential thermogravimetry analysis (DTA)

Thermogravimetric analysis (TGA) and DTA of synthesized MgO xerogel were conducted by means of a transverse acoustic (TA) TGA-SDT Q600 analyser in order to evaluate kinetic and thermodynamic properties. The sample weight was around 14 mg and placed in an alumina crucible. The temperature was raised from the ambient temperature up to 800 °C with various heating rates (2, 5, 10, and 20 °C/min) under an air atmosphere.

2.2.2 Kinetic analysis methods

TGA/DTA measurements under different heating rates were carried out, as explained in Section 2.2.1. The rate of kinetic process in non-isothermal transformation is frequently expressed, as seen in Eq. (1).

$$\frac{d\alpha}{dt} = k(T)f(\alpha) \quad (1)$$

where α is the fractional conversion factor and can be calculated from experimental TGA data. The formulation of α is equivalent to $(m_i - m_t)/(m_i - m_e)$, and m_i , m_t , and m_e are the initial mass, mass at time t , and final mass of the sample, respectively. $k(T)$ is the rate constant, which is defined by the Arrhenius equation, $k(T) = A \exp(-E/RT)$. Where E is the activation energy, A is the pre-exponential factor, T and R are temperature and gas constant, respectively. Substituting the Arrhenius equation in Eq. (1) and using β (dT/dt), which is a constant heating rate for measurements, the differential form of the rate law can be written as expressed

Eq. (2) [32].

$$\frac{d\alpha}{dT} = \frac{A}{\beta} \exp\left(-\frac{E_a}{RT}\right) f(\alpha) \quad (2)$$

TGA/DTA data can be evaluated based on model-fitting and/or model-free methods derived from Eq. (2). The results were evaluated using model-free methods in order to determine the kinetic parameters such as E_a and A . There are several model-free methods, such as Flynn–Wall–Ozawa (FWO) [33–36], Kissinger–Akahira–Sonuse (KAS) [37–39], Starink [40], and Tang methods [41].

2.2.2.1 FWO method The FWO method allows obtaining the activation energy, E_a from a plot of $\log\beta$ versus $1/T$.

$$\ln\beta = \ln\left[\frac{AE_a}{Rg(\alpha)}\right] - 5.331 - 1.052 \frac{E_a}{RT} \quad (3)$$

2.2.2.2 KAS method A plot of $\ln\left(\frac{\beta}{T^2}\right)$ versus $1/T$ gives a slope of E_a/R .

$$\ln\left(\frac{\beta}{T^2}\right) = \ln\left[\frac{AR}{E_a g(\alpha)}\right] - \frac{E_a}{RT} \quad (4)$$

2.2.2.3 Starink method Starink method, Eq. (5), is one of the iso-conversional models and is suggested as a more precise approximation than both of KAS and FWO methods [40, 42]

$$\ln\left(\frac{\beta}{T^{1.92}}\right) = \ln\left[\frac{AR^{0.92}}{E_a^{0.92} g(\alpha)}\right] - 0.312 - 1.0008 \frac{E_a}{RT} \quad (5)$$

where $C_{Starink}$ is a constant. The activation energy, E_a , can be determined slope of $\ln\left(\frac{\beta}{T^{1.92}}\right)$ against $1/T$ graph.

2.2.2.4 Tang method Tang method is a modified method of the Madhusudanan–Krishnan–Ninan method [43] and the relation $\ln\left(\frac{\beta}{T^{1.894661}}\right)$ to $1/T$ is represented as seen below.

$$\ln\left(\frac{\beta}{T^{1.894661}}\right) = \ln\left[\frac{A}{g(\alpha)} \left(\frac{E_a}{R}\right)^{-0.894661}\right] - 0.37773896 - 1.00145033 \frac{E_a}{RT} \quad (6)$$

The thermodynamic parameters such as standard entropy (ΔS), standard enthalpy (ΔH), and standard Gibbs free energy (ΔG) were determined using Eqs. (7)–(9) [44],

$$\ln A - \frac{E_a}{RT_P} = \ln \frac{kT_P}{h} - \frac{\Delta G}{RT_P} \quad (7)$$

$$\Delta H = E_a - RT_P \quad (8)$$

$$\Delta G = \Delta H - T_P \Delta S \quad (9)$$

where k is the Boltzmann constant and h is the Planck's constant. T_p is the peak temperature.

2.2.3 Characterization methods

XRD analysis of MgO powders was carried out by the Panalytical Empyrean XRD instrument using Cu K α radiation (1.5406 Å). Scanning electron microscopy (SEM) examinations of MgO powders were investigated by means of Carl Zeiss 300 VP instrument. Specific surface areas and pore sizes of MgO particles were determined by Brunauer–Emmett–Teller (BET) method using the N₂ adsorption/desorption at 77 K with Micromeritics 3Flex surface area analyser. Raman analysis of powders was performed via the Renishaw Invia Raman system. PL emission spectra were obtained using FS5 spectrofluorometer Edinburgh Instruments.

2.3 Antibacterial studies

The agar disc diffusion method was employed in order to investigate the antibacterial activities of MgO samples. The antibacterial performance was studied against gram-negative *Escherichia coli* (*E. Coli*) and gram-positive *Bacillus subtilis* (*B. Subtilis*) bacteria. A total of 150 mg of MgO powder was transferred to the 13 mm mold and pressed under 300 kPa to form a tablet. In the agar disc diffusion method, the stock solution of 0.5 ml of both bacteria was inoculated for each sample. The stock bacteria solutions were transferred to nutrient agar and incubated in order to get 10⁸ CFU/ml concentration cell culture at 37 °C for 24 h. The prepared MgO samples were placed on the surface of the cultured agar plates and incubated at 37 °C for 24 h to observe inhibition zones around to samples. The inhibition zone is the area in which the bacterial growth is stopped. The diameter of the inhibition zones was measured in millimeter. Also, the control samples were prepared for both *E. coli* and *B. Subtilis* without adding any MgO particles.

3 Result and discussion

3.1 Non-isothermal kinetics

The TG curves of MgO powders were presented in Fig. 1, which shows that the weight loss of the MgO powders is ~50% between 300 and 500 °C. This result fits the results of Jeevanandam et al. [29]. They revealed that the weight loss changed between ~52 and 67% depending on the type of gelling agent used to produce MgO particles. The change in temperature values is related to the heating rate (2–20 °C/min). The TGA curves shifted to a higher temperature

region with increasing the heating rate. As explained in Section 2, four model-free methods, i.e., FWO, KAS, Starink, and Tang methods, were applied to determine the activation energy, E_a at four different heating rates. The plots for the model-free methods were illustrated in Fig. 2. According to Eqs. (3)–(6), the calculated activation energy (E_a) was listed in Table 1 for each model-free technique. Even though the models caused the small differences in the activation energy values, the close values indicated that the E_a values were acceptable. Moreover, it can be seen that the values decreased with increasing the conversion rate from 0.1 to 0.9. However, there are small differences between the results related to the various mathematical formulations of the models. The thermodynamic properties such as Gibbs free energy (ΔG), enthalpy (ΔH), and entropy (ΔS) were calculated by using Eqs. (7)–(9). The results calculated at T_p were listed in Table 2. The corresponding average values for ΔG , ΔH , and ΔS were determined as 179.52, 204.19 kJ/mol, and 37.01 J/(molK), respectively. The positive ΔH and ΔG values indicated that the thermal decomposition of MgO powders was an endothermic non-spontaneous reaction. Also, ΔH is >0, and ΔS is >0, which means that the process needs heat energy to proceed spontaneously.

3.2 XRD analysis

XRD patterns of the MgO powders were illustrated in Fig. 3. The locations of the peaks were characteristics of MgO representing (111), (200), (220), (311), and (222) sets of lattice planes according to the standard reference file (JCPDS 98-015-9369). There are more lattice planes, which indicate the polycrystallinity of the fabricated MgO samples. The sharp XRD peaks were indicative of highly crystalline MgO particles regardless of the heating rate.

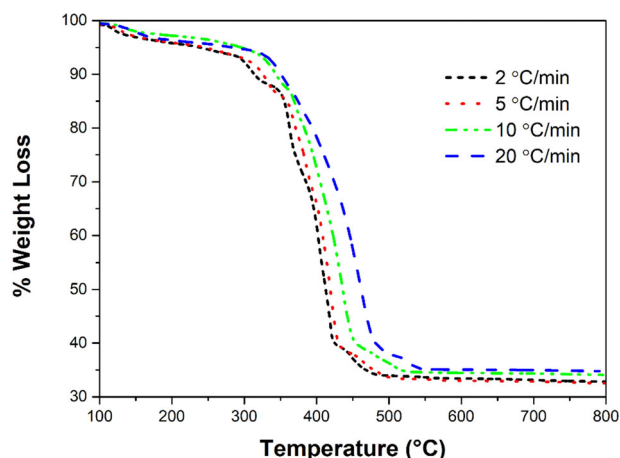


Fig. 1 TGA curves of the prepared MgO powders at different heating rates under air atmosphere

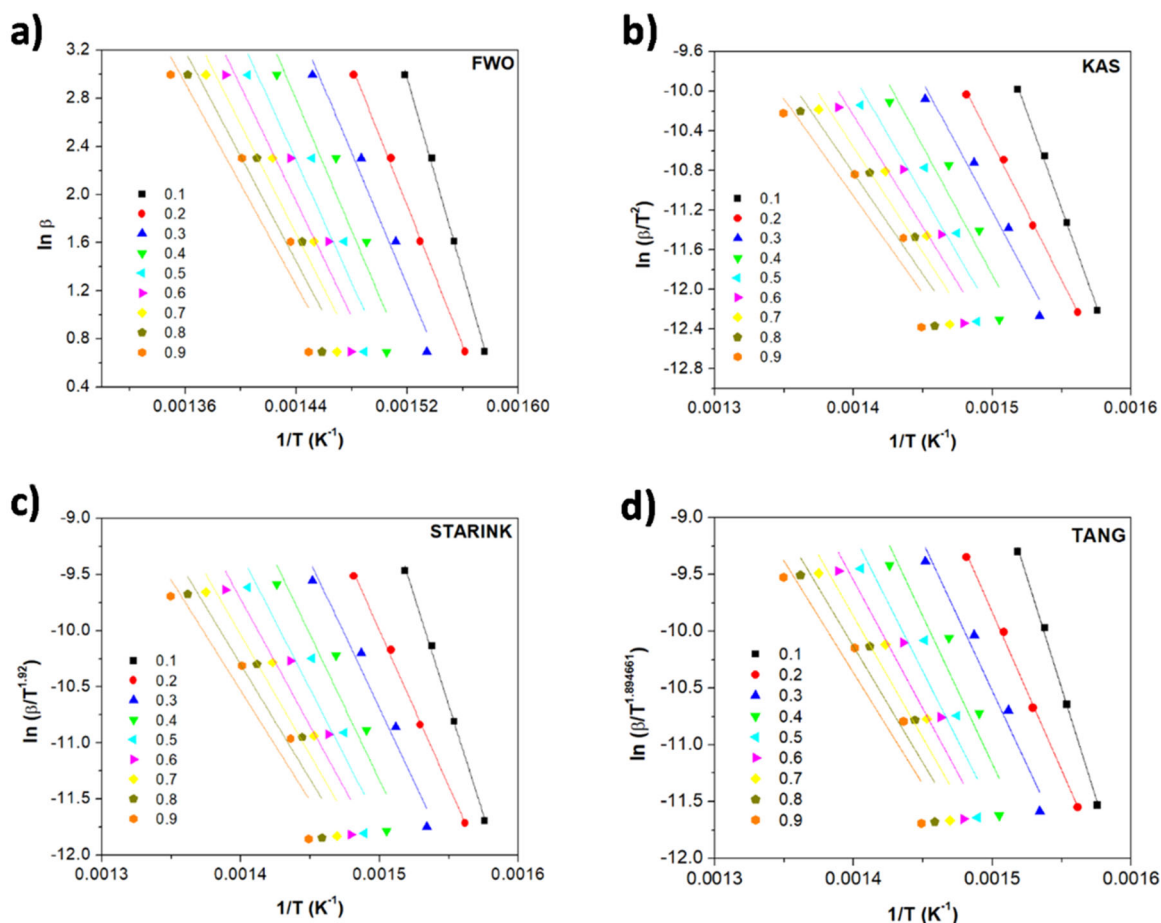


Fig. 2 The curves of the FWO, KAS, Starink, and Tang model-free models for thermodynamic calculations

Table 1 Activation energies based on FWO, KAS, Starink, and Tang methods

α	FWO		KAS		Starink		Tang	
	Activation energy (E_a) (kJ/mol)	LnA (s^{-1})	Activation energy (E_a) (kJ/mol)	LnA (s^{-1})	Activation energy (E_a) (kJ/mol)	LnA (s^{-1})	Activation energy (E_a) (kJ/mol)	LnA (s^{-1})
0.1	318.94	56.83	324.77	57.68	324.94	57.75	324.86	57.73
0.2	229.69	39.68	230.71	39.84	230.96	39.93	230.95	39.92
0.3	216.99	37.11	217.13	37.10	217.40	37.20	217.40	37.20
0.4	215.30	36.51	215.14	36.45	215.42	36.55	215.43	36.55
0.5	201.13	33.80	200.08	33.57	200.39	33.68	200.40	33.68
0.6	189.02	31.59	187.24	31.22	187.56	31.33	187.58	31.34
0.7	179.75	29.96	177.40	29.46	177.72	29.58	177.75	29.59
0.8	172.63	28.76	169.80	28.17	170.13	28.29	170.17	28.30
0.9	166.16	27.78	162.90	27.09	163.25	27.22	163.30	27.23
Average	209.96	35.78	209.46	35.62	209.75	35.73	209.76	35.73

The absence of any other peaks substantiated the purity of the calcined MgO powders. The XRD results in our study supported the literature work [45]. The crystallite size (D) of the MgO particles was estimated using the following

Derby–Scherrer equation [46].

$$D = \frac{k\lambda}{\beta \cos\theta} \tag{10}$$

where $k = 0.94$, $\lambda = 1.5418 \text{ \AA}$, $\beta =$ full width half maximum (FWHM) and $\theta =$ diffracting angle. In addition to crystallite size, dislocation density (δ) was calculated by the equation [10].

$$\delta = 1/D^2 \quad (11)$$

The crystalline size and dislocation density of the prepared MgO particles were given in Table 3. The value of the crystalline size of MgO particles was highly small, which indicates the high degree of crystallinity. XRD results supported the presence of high crystalline phases. Further-

Table 2 Thermodynamic parameters for thermal decomposition of the MgO particles

β ($^{\circ}\text{C}/\text{min}$)	ΔH (kJ/mol)	ΔG (kJ/mol)	ΔS (J/molK)	T_p ($^{\circ}\text{C}$)
2	204.40	180.48	37.34	367.69
5	204.23	179.72	37.08	388.12
10	204.09	179.10	36.87	405.01
20	204.02	178.76	36.75	414.34
Average	204.19	179.52	37.01	

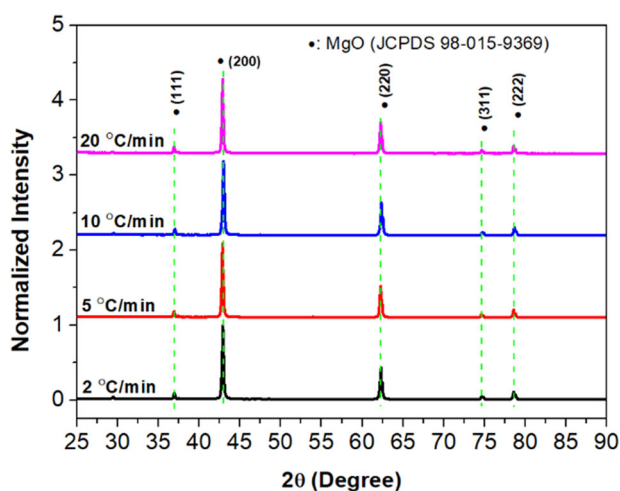


Fig. 3 XRD patterns of the MgO powders calcined at 600 $^{\circ}\text{C}$ for 2 h at different thermal treatment route

Table 3 Crystallographic information and physical properties of MgO powders calcined at 600 $^{\circ}\text{C}$ for 2 h at different heating rate

Samples	Microstructure				
	Lattice parameter (\AA)	Crystalline size (nm)	Dislocation density ($\delta \times 10^{15} \frac{\text{lines}}{\text{m}^2}$)	Lattice strain ($(\times 10^{-6}) \epsilon$)	S_{BET} (m^2g^{-1})
2 $^{\circ}\text{C}/\text{min}$	4.21793	9.29	11.5	6.63	5.9179
5 $^{\circ}\text{C}/\text{min}$	4.21645	10.29	9.44	2.75	5.6883
10 $^{\circ}\text{C}/\text{min}$	4.21816	8.6	13.52	0.0158	3.6617
20 $^{\circ}\text{C}/\text{min}$	4.21683	10.49	9.08	0.365	4.1942

more, the dislocation density value illustrates the degree of crystallinity. Small dislocation density value implies that MgO particles showed a high degree of crystallinity.

3.3 Surface morphology of MgO particles

SEM images of the calcined MgO powders were presented in Fig. 4. Surface morphologies of the powders were found to be nearly spherical with some rounded shape and exhibiting faceted edges in some regions. The sphere-like morphology of MgO particles became more evident at a high heating rate, 20 $^{\circ}\text{C}/\text{min}$. Some degree of agglomeration was also observed, which was a bit more for the lowest heating rate, 2 $^{\circ}\text{C}/\text{min}$. The surface morphology of the particles was similar with some other studies [8, 47]. The size of the particles showed no trend between different heating rates in a proportional manner. The average of the particle size for each SEM image is shown in Fig. 4. Average particle sizes of MgO particles obtained for 2, 5, 10, and 20 $^{\circ}\text{C}/\text{min}$ heating rate were determined to be 378.3 ± 91.2 , 489.0 ± 122.5 , 385.6 ± 38.7 , and 448.8 ± 51.3 nm, respectively. Based on the findings, it could be deduced that MgO particles became more homogenous with increasing heating rate.

3.4 BET analysis

BET analysis was implemented in order to quantify specific surface areas of MgO powders produced at different thermal treatment route. The N_2 adsorption–desorption isotherms of MgO particles and their pore size distribution, which were embedded in N_2 adsorption–desorption isotherms, were shown in Fig. 5. As can be seen in Fig. 5, the N_2 adsorption isotherms of MgO particles took place at relative pressure (P/P_0) between 0.8 and 1. The isotherm behaviors of MgO particles might be categorized as type IV isotherm with the H3 hysteresis loop according to the IUPAC classification [48]. Based on the N_2 adsorption–desorption isotherm curves, the specific surface area of the fabricated MgO powders was found to be (a) 5.9179 m^2/g , (b) 5.6883 m^2/g , (c) 3.6617 m^2/g , and (d) 4.1942 m^2/g with increasing heating rate, respectively. These small BET surface area values are in agreement with the study of Du et al. [49].

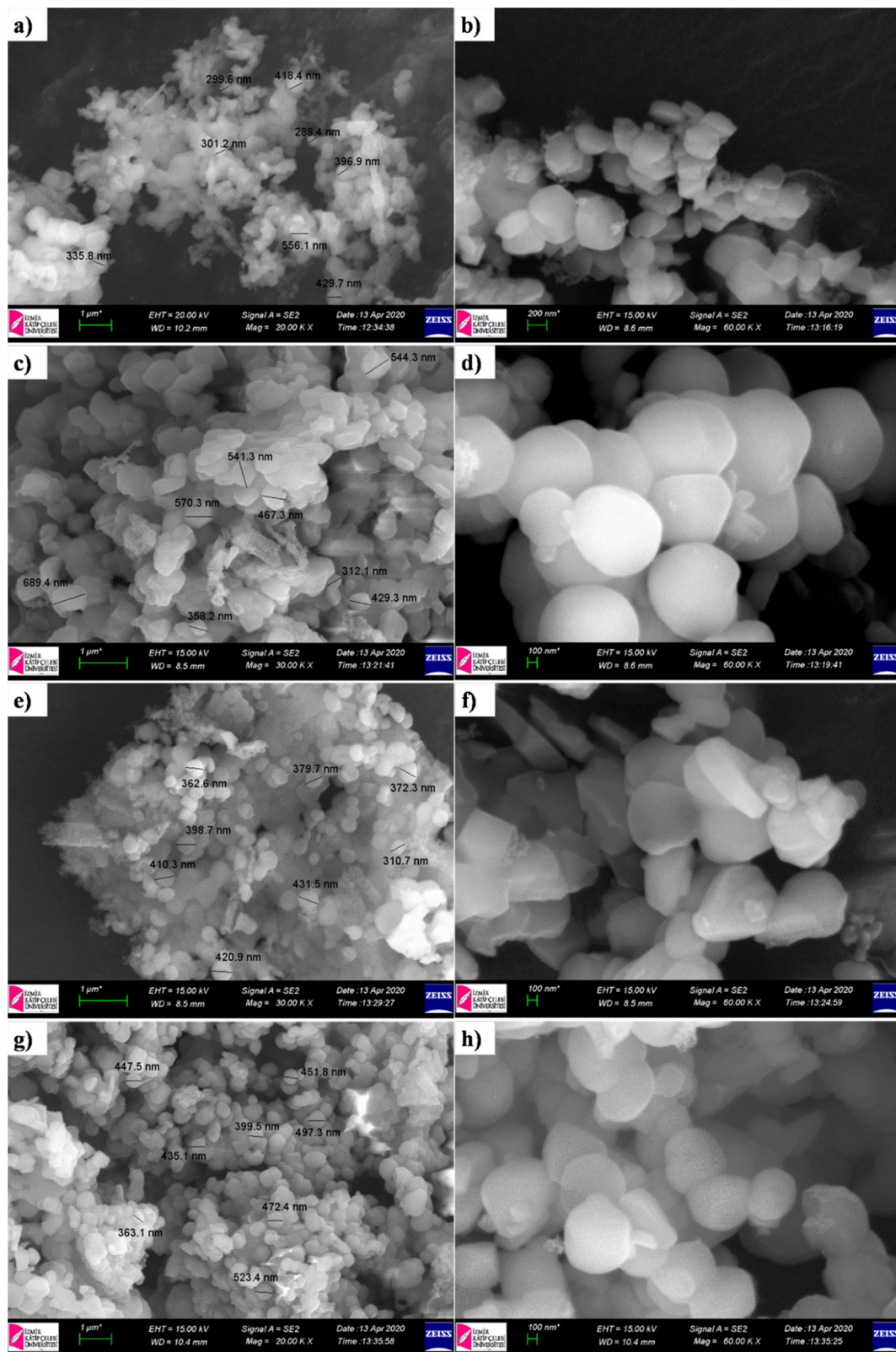


Fig. 4 SEM images of the MgO powders calcined at 600 °C for 2 h at different heating rates **a, b** 2 °C/min, **c, d** 5 °C/min, **e, f** 10 °C/min, **g, h** 20 °C/min

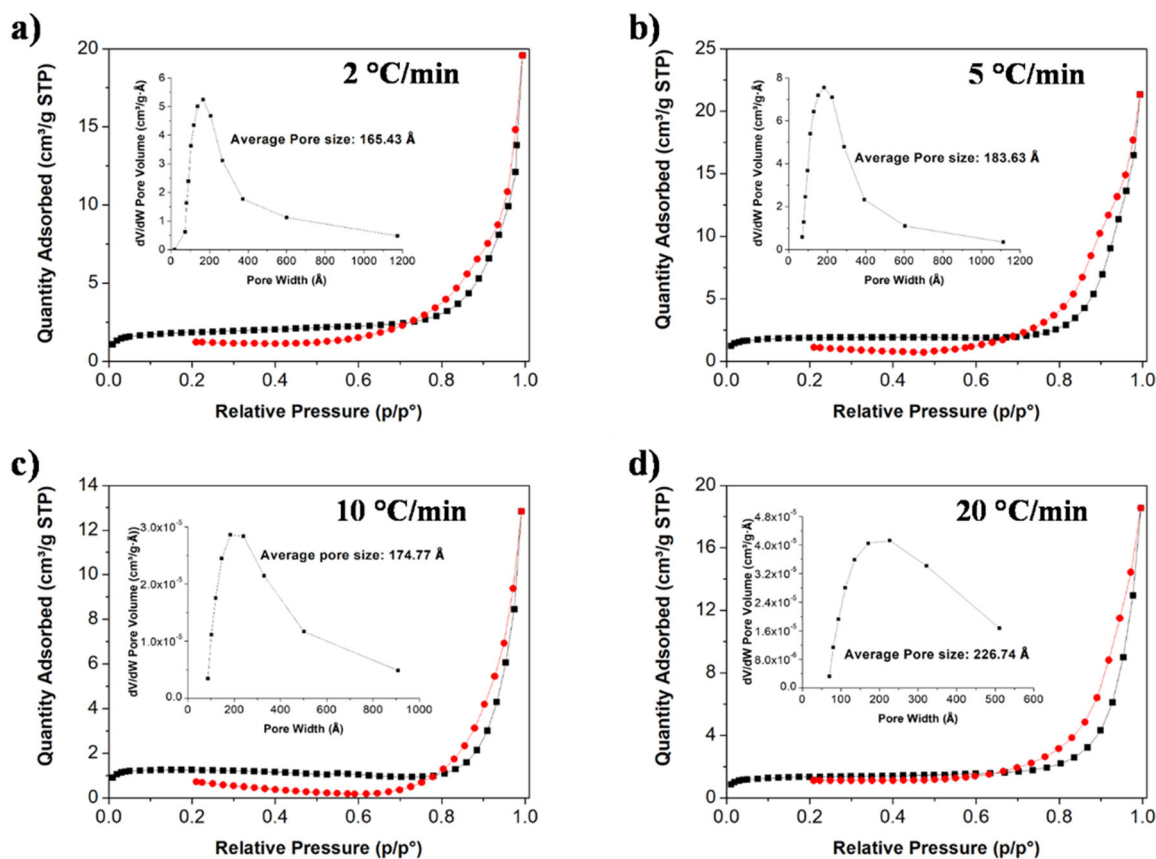


Fig. 5 N_2 adsorption–desorption isotherms for MgO particles and their pore size distribution (embedded). Nitrogen adsorption and desorption isotherms measured at 77 K for MgO powders prepared at different thermal treatment route

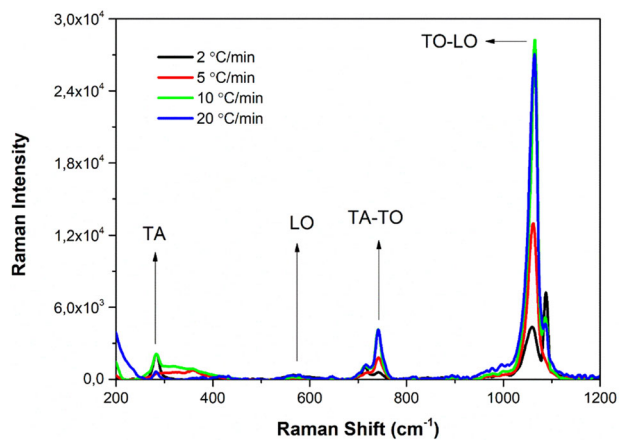


Fig. 6 Raman spectra of MgO particles between 200 and 1200 cm^{-1} , which were annealed at 2, 5, 10, and 20 $^{\circ}C/min$ heating rate

Furthermore, the pore size distributions of the prepared particles were embedded in the N_2 adsorption–desorption isotherm curves. The average pore size for MgO particles was determined so as to be 16.5, 18.36, 17.47, and 22.64 nm. It reveals that the fabricated MgO particles were mesoporous materials. If the pore size of the material is

between 5 and 50 nm, the material is called mesoporous material, according to the IUPAC classification [48]. It reveals that the fabricated MgO particles were mesoporous materials.

3.5 Raman spectra of MgO particles

Raman spectra of MgO particles were performed in the range of 100–1200 cm^{-1} shown in Fig. 6. The bulk MgO does not have a Raman spectrum because of its inversion symmetry [50]. The observed Raman signals are only related to the surface information. The Raman peak observed around 282 cm^{-1} should be related to TA phonon at the nanostructure zone boundary [51]. The observed Raman peaks near 564 cm^{-1} were associated with longitudinal optical (LO) mode of MgO particles [52]. The Raman modes of transversal acoustics (TA) and transverse optical (TO) for MgO particles were seen at 742 cm^{-1} [53]. The highest peaks around 1064 cm^{-1} accompanying with shoulder peaks near 1086 cm^{-1} might be attributed to TO–LO modes due to surface phonon gap [54]. The intensity and FWHM of Raman spectra are often used as an indication of the ordering in the material. The presence of

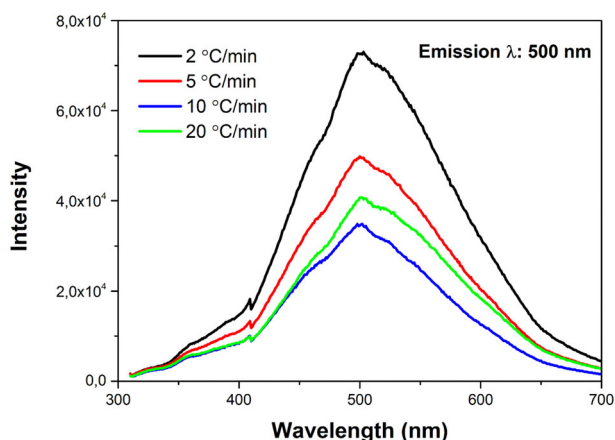


Fig. 7 PL emission spectra of MgO powders prepared at various thermal treatment route

lower intense Raman peaks means having a higher degree of disorder (vacancies or defects) in the material's surface. Within this framework, the disorder on the surface, which means that oxygen defects and vacancies, decreased by increasing the heating rate. So that, MgO produced at 2 °C/min possessed lower intense Raman signal. Therefore, it had higher surface defects, like oxygen vacancies. The PL analysis supported this result.

3.6 PL studies

The PL studies for produced MgO powders at different thermal treatment routes were performed to figure out and understand bulk and surface defects. The PL emission spectra of particles were obtained after an excitation wavelength of 360 nm. The PL emission signals were observed at ~500 nm consisting of broad peaks, as given in Fig. 7. The observed broad emission of PL centered at almost 500 nm might be attributed to the recombination of electrons and surface oxygen defects or vacancies on the surface of produced powders [13, 55–57]. The increase in intensity of PL emission spectra implies an increase of surface oxygen defects. Within this concept, it was clearly seen in Fig. 7 that the surface oxygen defects for MgO particles showed a decreasing trend with increasing heating rate. It could be concluded that the MgO particles produced at 2 °C/min had the highest surface oxygen defects, while the lowest was MgO particles produced at 10 °C/min. Having high surface defects is very crucial for antibacterial application. Higher surface defects enable to generate much more ROS.

3.7 Antibacterial studies

As can be seen in Fig. 8, the antibacterial performances of MgO particles were carried out against gram-negative

E. coli and gram-positive *B. subtilis* by means of the agar disc diffusion method. The zone of inhibition areas around the samples was measured in millimeter. The areas around the samples indicate that no bacterial growth occurs. In other words, the growth of bacteria is limited. The inhibition zone values (in mm) for MgO particles were given in Table 4. MgO particles showed better inhibition in the growth against gram-positive *B. subtilis* as compared to gram-negative *E. coli*. The MgO particles produced at 2 °C/min heating rate possessed the biggest inhibition zone against gram-positive *B. subtilis*. The inhibition zone diameter for MgO particles produced at a heating rate of 2 °C/min was 3.9 mm. The MgO particle fabricated at 10 °C/min heating rate showed the lowest antibacterial activity toward the *B. subtilis*. This sample had an inhibition zone of 2 mm in diameter. When it comes to gram-negative *E. coli* bacterium, the MgO samples did not show the desired antibacterial activity. The existing one can be neglected. The result of antibacterial activity clearly showed that the antibacterial performance of MgO particles was in the following order: MgO (2 °C/min) > MgO (5 °C/min) > MgO (20 °C/min) > MgO (10 °C/min) against gram-positive *B. subtilis*. The antibacterial activity of MgO samples is generally related to ROS, which may originate from the specific surface area, morphology, degree of crystallinity, crystal size, surface oxygen vacancies, and diffusion capability of chemical compounds [10]. In our study, the discrepancy in antibacterial performances for MgO particles might be ascribed from surface oxygen vacancies and surface area. Even though the specific surface areas of MgO samples were very close to each other, MgO particles produced at 2 °C/min heating rate had the highest surface area, which permits them to interact with the cell membrane of the bacteria through its surface. The more interaction between the bacterium and sample prevents the growth of bacteria because of having more reactive surface oxygen vacancies. The oxygen vacancies on the surface of MgO particles adsorb oxygen (O_2) originated from bacteria and produce ROS based on the following reactions below such as superoxide radicals (O_2^-), hydroxyl radicals ($\cdot OH$), and hydrogen peroxide (H_2O_2), which cause oxidative stress on bacterial cells. The strong oxidative stress causes damage to the biological system in order to destroy and kill them [58, 59].

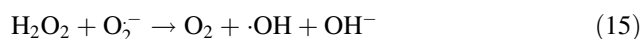
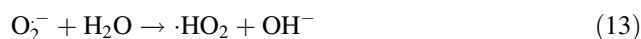
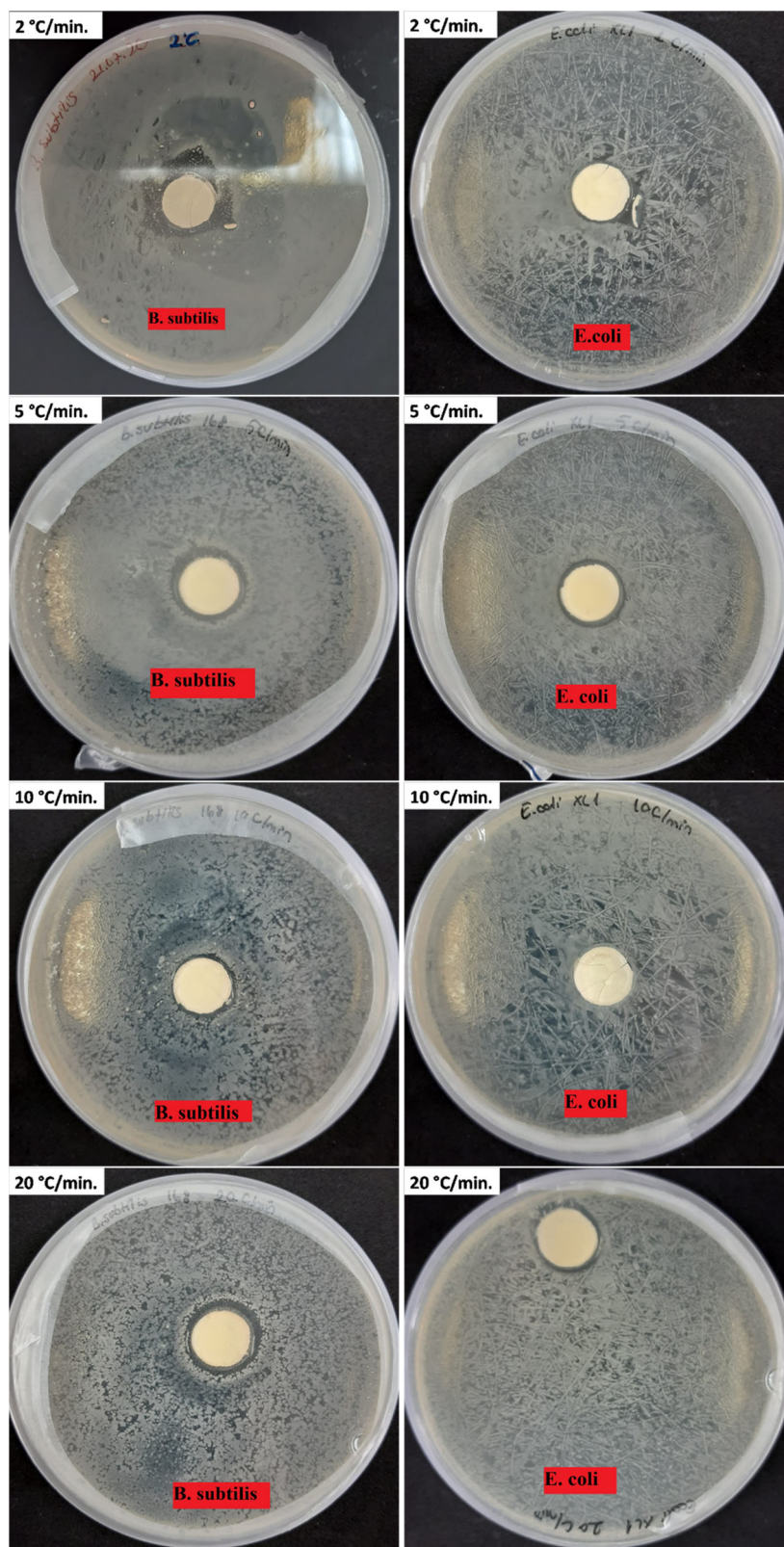


Fig. 8 Antibacterial activities of MgO powders against *B. subtilis* and *E. coli* bacteria tested by Agar well diffusion method. The inhibition zones are clearly seen in both the cases



The adsorbed oxygen molecules are transformed into superoxide anion radical (O_2^-) after reaction with electrons. Then, superoxide radicals react with water to generate

hydroperoxyl radicals. After the formation of hydroperoxyl radicals, they can recombine to form H_2O_2 . The formed H_2O_2 may react with superoxide radical to form hydroxyl

Table 4 Inhibition zone measure in (mm) for MgO particles prepared at various heating rate

Bacterial species	2 °C/min	5 °C/min	10 °C/min	20 °C/min
<i>B. subtilis</i>	3.9 mm	1.4 mm	1.0 mm	1.5 mm
<i>E. coli</i>	1.1 mm	1.1 mm	0.7 mm	0.8 mm

radical and hydroxyl ion. Finally, the generated H_2O_2 reacts with superoxide anion radical and form hydroxyl radical and hydroxyl ion. The generated ROS play an important role in antibacterial activity [59]. Within this framework, it can be deduced that MgO particles produced at 2 °C/min heating rate had the highest surface oxygen vacancies according to our Raman and PL analysis. Hence, the antibacterial activity of MgO particles produced at 2 °C/min heating rate was better than the others because of the production of more ROS.

4 Conclusion

In conclusion, MgO particles were prepared by means of the sol-gel route and calcined at 600 °C for 2 h with distinct heating rates. XRD patterns showed that MgO samples exhibited a high crystalline structure. Surface morphologies of MgO powders were found to be nearly spherical with some rounded shape and exhibiting faceted edges in some regions. The average particle size varied from 378 to 480 nm for MgO powders. The specific surface area of MgO powders was found to be 5.9179, 5.6883, 3.6617, and 4.1942 m²/g by an increase in heating rate, respectively. MgO particles produced at 2 °C/min possessed higher surface defects, like oxygen vacancies. The antibacterial performances of MgO particles were carried out against gram-negative *E. coli* and gram-positive *B. subtilis* by means of the agar disc diffusion method. MgO particles produced at 2 °C/min heating rate possessed the biggest inhibition zone against gram-positive *B. subtilis*. The diameter of the inhibition zone for MgO particles produced at a heating rate of 2 °C/min was 3.9 mm. In sum, MgO particles should be a good candidate for antimicrobial-based applications. It is recommended for the further studies to investigate the effect of the calcination temperature on modification of the shape, size, antibacterial activity, etc. of MgO particles.

Acknowledgements The authors are indebted to Marmara University and Katip Çelebi University for infrastructural support.

Compliance with ethical standards

Conflict of interest The authors declare no competing interests.

Publisher's note Springer Nature remains neutral with regard to jurisdictional claims in published maps and institutional affiliations.

References

- Raghunath A, Perumal E (2017) Metal oxide nanoparticles as antimicrobial agents: a promise for the future. *Int J Antimicrobial Agents* 49:137–152
- Wong CW, Chan YS, Jeevanandam J, Pal K, Bechelany M, Abd Elkodous M, El-Sayyad GS (2020) Response surface methodology optimization of mono-dispersed MgO nanoparticles fabricated by ultrasonic-assisted sol-gel method for outstanding antimicrobial and antibiofilm activities. *J Clust Sci* 31:367–389
- Srivastava V, Sharma YC, Sillanpää M (2015) Green synthesis of magnesium oxide nanoflower and its application for the removal of divalent metallic species from synthetic wastewater. *Ceram Int* 41:6702–6709
- Savita Jain M, Manju, Vij A, Thakur A (2019) Impact of annealing on the structural properties of MgO nanoparticles by XRD analysis and Rietveld refinement. *AIP Conf Proc* 2093:020024
- Rao Y, Wang W, Tan F, Cai Y, Lu J, Qiao X (2013) Influence of different ions doping on the antibacterial properties of MgO nanopowders. *Appl Surf Sci* 284:726–731
- Jin X, Yuan K, Lin X, Wang X, Zhang G, Zhu L, Que N, Xu D (2018) Effects of water vapor on the crystallization and microstructure manipulation of MgO ceramic fibers. *Ceram Int* 44:5257–5265
- Yang C, Wang Y, Fan H, de Falco G, Yang S, Shangguan J, Bandosz TJ (2020) Bifunctional ZnO-MgO/activated carbon adsorbents boost H₂S room temperature adsorption and catalytic oxidation. *Appl Catal B: Environ* 266:118674
- Demirci S, Öztürk B, Yildirim S, Bakal F, Erol M, Sancakoğlu O, Yigit R, Celik E, Batar T (2015) Synthesis and comparison of the photocatalytic activities of flame spray pyrolysis and sol-gel derived magnesium oxide nano-scale particles. *Mater Sci Semicond Process* 34:154–161
- Shafiee H, Salehirad A, Samimi A (2020) Effect of synthesis method on structural and physical properties of MgO/MgAl₂O₄ nanocomposite as a refractory ceramic. *Appl Phys A* 126:198
- Karthik K, Dhanuskodi S, Gobinath C, Prabukumar S, Sivaramakrishnan S (2019) Fabrication of MgO nanostructures and its efficient photocatalytic, antibacterial and anticancer performance. *J Photochem Photobiol B: Biol* 190:8–20
- Srisuvetha VT, Rayar SL, Shanthi G (2020) Role of cerium (Ce) dopant on structural, optical and photocatalytic properties of MgO nanoparticles by wet chemical route. *J Mater Sci: Mater Electron* 31:2799–2808
- Cai Y, Li C, Wu D, Wang W, Tan F, Wang X, Wong PK, Qiao X (2017) Highly active MgO nanoparticles for simultaneous bacterial inactivation and heavy metal removal from aqueous solution. *Chem Eng J* 312:158–166
- El-Shaar A, Abdelfatah M, Mahmoud KR, Momay S, Eraky MR (2020) Correlation between photoluminescence and positron annihilation lifetime spectroscopy to characterize defects in calcined MgO nanoparticles as a first step to explain antibacterial activity. *J Alloy Compd* 817:152799
- Dizaj SM, Lotfipour F, Barzegar-Jalali M, Zarrintan MH, Adibkia K (2014) Antimicrobial activity of the metals and metal oxide nanoparticles. *Mater Sci Eng: C* 44:278–284
- Anićić N, Vukomanović M, Koklič T, Suvorov D (2018) Fewer defects in the surface slows the hydrolysis rate, decreases the ROS generation potential, and improves the non-ROS antimicrobial activity of MgO. *Small* 14:1800205

16. Leung YH, Ng AMC, Xu X, Shen Z, Gethings LA, Wong MT, Chan CMN, Guo MY, Ng YH, Djurišić AB, Lee PKH, Chan WK, Yu LH, Phillips DL, Ma APY, Leung FCC (2014) Mechanisms of antibacterial activity of MgO: non-ROS mediated toxicity of MgO nanoparticles towards *Escherichia coli*. *Small* 10:1171–1183
17. Li Y, Zhang W, Niu J, Chen Y (2012) Mechanism of photo-generated reactive oxygen species and correlation with the antibacterial properties of engineered metal-oxide nanoparticles. *ACS Nano* 6:5164–5173
18. Ning P, Zhang F, Wang LJ, Zhou Y, Wang YJ, Wu YY, Fu T (2020) Sol-gel derived AgMgO films for antibacterial and bioactive surface modification of niobium metal. *Mater Chem Phys* 243:122646
19. Makhluף S, Dror R, Nitzan Y, Abramovich Y, Jelinek R, Gedanken A (2005) Microwave-assisted synthesis of nanocrystalline MgO and its use as a bactericide. *Adv Funct Mater* 15:1708–1715
20. Sabbaghan M, Sofalgar P, Zarinejad M (2020) Ionic liquid-based controllable synthesis of MgO nanostructures for high specific surface area. *Ceram Int* 46:6940–6944
21. Yan X, Tian Z, Peng W, Zhang J, Tong Y, Li J, Sun D, Ge H, Zhang J (2020) Synthesis of nano-octahedral MgO via a solvothermal-solid-decomposition method for the removal of methyl orange from aqueous solutions. *RSC Adv* 10:10681–10688
22. Rao LS, Rao TV, Naheed S, Rao PV (2018) Structural and optical properties of zinc magnesium oxide nanoparticles synthesized by chemical co-precipitation. *Mater Chem Phys* 203:133–140
23. Karthik K, Dhanuskodi S, Prabu Kumar S, Gobinath C, Sivaramakrishnan S (2017) Microwave assisted green synthesis of MgO nanorods and their antibacterial and anti-breast cancer activities. *Mater Lett* 206:217–220
24. Lu X, Kanamori K, Nakanishi K (2019) Synthesis of hierarchically porous MgO monoliths with continuous structure via sol-gel process accompanied by phase separation. *J Sol-Gel Sci Technol* 89:29–36
25. Li S (2019) Combustion synthesis of porous MgO and its adsorption properties. *Int J Ind Chem* 10:89–96
26. Aničić N, Vukomanović M, Suvorov D (2016) The nano-texturing of MgO microrods for antibacterial applications. *RSC Adv* 6:102657–102664
27. Cai Y, Wu D, Zhu X, Wang W, Tan F, Chen J, Qiao X, Qiu X (2017) Sol-gel preparation of Ag-doped MgO nanoparticles with high efficiency for bacterial inactivation. *Ceram Int* 43:1066–1072
28. Wang Y, Cen C, Chen J, Fu L (2020) MgO/carboxymethyl chitosan nanocomposite improves thermal stability, waterproof and antibacterial performance for food packaging. *Carbohydr Polym* 236:116078
29. Jeevanandam J, Chan YS, Danquah M (2019) Effect of gelling agent and calcination temperature in sol-gel synthesized MgO nanoparticles. *Prot Met. Phys Chem* 55:288–301
30. Dikici T, Demirci S, Tünçay MM, Yildirim BK, Kaya N (2021) Effect of heating rate on structure, morphology and photocatalytic properties of TiO₂ particles: thermal kinetic and thermodynamic studies. *J Sol-Gel Sci Technol* 97:622–637
31. Demirci S, Dikici T, Tünçay MM, Kaya N (2020) A study of heating rate effect on the photocatalytic performances of ZnO powders prepared by sol-gel route: Their kinetic and thermodynamic studies. *Appl Surf Sci* 507:145083
32. White JE, Catallo WJ, Legendre BL (2011) Biomass pyrolysis kinetics: a comparative critical review with relevant agricultural residue case studies. *J Anal Appl Pyrolysis* 91:1–33
33. Doyle CD (1962) Estimating isothermal life from thermogravimetric data. *J Appl Polym Sci* 6:639–642
34. Takeo O (1965) A new method of analyzing thermogravimetric data. *Bull Chem Soc Jpn* 38:1881–1886
35. Flynn JH, Wall LA (1966) A quick, direct method for the determination of activation energy from thermogravimetric data. *J Polym Sci Part B: Polym Lett* 4:323–328
36. Flynn JH (1983) The isoconversional method for determination of energy of activation at constant heating rates. *J Therm Anal* 27:95–102
37. Huang J-W, Chang C-C, Kang C-C, Yeh M-Y (2008) Crystallization kinetics and nucleation parameters of Nylon 6 and poly(ethylene-co-glycidyl methacrylate) blend. *Thermochim Acta* 468:66–74
38. Kissinger HE (1957) Reaction kinetics in differential thermal analysis. *Anal Chem* 29:1702–1706
39. Chaiwang P, Chalerm-sinsuwan B, Piumsomboon P (2016) Thermogravimetric analysis and chemical kinetics for regeneration of sodium and potassium carbonate solid sorbents. *Chem Eng Commun* 203:581–588
40. Starink MJ (2003) The determination of activation energy from linear heating rate experiments: a comparison of the accuracy of isoconversion methods. *Thermochim Acta* 404:163–176
41. Tang W, Liu Y, Zhang H, Wang C (2003) New approximate formula for Arrhenius temperature integral. *Thermochim Acta* 408:39–43
42. Pourmortazavi SM, Mirzajani V, Farhadi K (2019) Thermal behavior and thermokinetic of double-base propellant catalyzed with magnesium oxide nanoparticles. *J Therm Anal Calorim* 137:93–104
43. Madhusudanan PM, Krishnan K, Ninan KN (1993) New equations for kinetic analysis of non-isothermal reactions. *Thermochim Acta* 221:13–21
44. Mahmood A, Tezcan F, Kardaş G (2018) Thermal decomposition of sol-gel derived Zn_{0.8}Ga_{0.2}O precursor-gel: a kinetic, thermodynamic, and DFT studies. *Acta Materialia* 146:152–159
45. Zhao X, Yang H, Wu P, Huang X, Wang X (2019) The preparation of MgO nanopowders synthesized via an improved polyacrylamide gel method. *RSC Adv* 9:14893–14898
46. Rani N, Chahal S, Chauhan AS, Kumar P, Shukla R, Singh SK (2019) X-ray analysis of MgO nanoparticles by modified Scherrer's Williamson-Hall and size-strain method. *Mater Today: Proc* 12:543–548
47. Umaralikhani L, Jamal Mohamed Jaffar M (2018) Green synthesis of MgO nanoparticles and its antibacterial activity. *Iran J Sci Technol, Trans A: Sci* 42:477–485
48. Sing KSW (1985) Reporting physisorption data for gas/solid systems with special reference to the determination of surface area and porosity (Recommendations 1984). *Pure Appl Chem* 57:603–619
49. Du L, Li Z, Ding S, Chen C, Qu S, Yi W, Lu J, Ding J (2019) Synthesis and characterization of carbon-based MgO catalysts for biodiesel production from castor oil. *Fuel* 258:116122
50. Hao Y-j, Liu B, Tian L-g, Li F-t, Ren J, Liu S-j, Liu Y, Zhao J, Wang X-j (2017) Synthesis of {111} facet-exposed MgO with surface oxygen vacancies for reactive oxygen species generation in the dark. *ACS Appl Mater Interfaces* 9:12687–12693
51. Krishnamoorthy K, Moon JY, Hyun HB, Cho SK, Kim S-J (2012) Mechanistic investigation on the toxicity of MgO nanoparticles toward cancer cells. *J Mater Chem* 22:24610–24617
52. Escobar-Alarcón L, Klimova T, Escobar-Aguilar J, Romero S, Morales-Ramírez C, Solís-Casados D (2013) Preparation and characterization of Al₂O₃-MgO catalytic supports modified with lithium. *Fuel* 110:278–285
53. Singh RK, Upadhyaya KS (1972) Crystal dynamics of magnesium oxide. *Phys Rev B* 6:1589–1596
54. Jaffar GH, Tahir A, Bah M, Ali A, Bhatti AS, Shah SI (2015) Study of surface-active modes and defects in single-phase Li-incorporated MgO nanoparticles. *J Phys Chem C* 119:28182–28189

55. Sellaiyan S, Uedono A, Sivaji K, Janet Priscilla S, Sivasankari J, Selvalakshmi T (2016) Vacancy defects and defect clusters in alkali metal ion-doped MgO nanocrystallites studied by positron annihilation and photoluminescence spectroscopy. *Appl Phys A* 122:920
56. Balakrishnan G, Velavan R, Mujasam Batoo K, Raslan EH (2020) Microstructure, optical and photocatalytic properties of MgO nanoparticles. *Results Phys* 16:103013
57. Arshad A, Iqbal J, Siddiq M, Mansoor Q, Ismail M, Mehmood F, Ajmal M, Abid Z (2017) Graphene nanoplatelets induced tailoring in photocatalytic activity and antibacterial characteristics of MgO/graphene nanoplatelets nanocomposites. *J Appl Phys* 121:024901
58. Thamilvanan D, Jeevanandam J, Hii YS, Chan YS (2021) Sol–gel coupled ultrasound synthesis of photo-activated magnesium oxide nanoparticles: optimization and antibacterial studies. *Can J Chem Eng* 99:502–518
59. Bhattacharya P, Dey A, Neogi S (2021) An insight into the mechanism of antibacterial activity by magnesium oxide nanoparticles. *J Mater Chem B* 9:5329–5339